# Sparse super-resolution phase retrieval from phase-coded noisy intensity patterns

**Vladimir Katkovnik**[1] *, **and Karen Egiazarian**[1]
[1]Laboratory of Signal Processing, Tampere University of Technology, P.O. Box 553 FI-33101 Tampere, Finland ,
Emails: vladimir.katkovnik@tut.fi, karen.egiazarian@tut.fi

**Abstract.** We consider computational super-resolution inverse diffraction problem for phase retrieval from phase-coded intensity observations. The optical setup includes a thin lens and a spatial light modulator (SLM) for phase coding. The designed algorithm is targeted on optimal solution for Poissonian noisy observations. One of the essential instruments of this design is a complex-domain sparsity applied for complex-valued object (phase and amplitude) to be reconstructed. Simulation experiments demonstrate that good quality imaging can be achieved for high-level of the super-resolution with factor 32, which means that the pixel of the reconstructed object is 32 times smaller than the sensor's pixel. This super-resolution corresponds to the object pixel as small as a quarter of the wavelength.

**Keywords:** Super-resolution, phase retrieval, complex domain sparsity, phase imaging, discrete optical signal processing.

* Corresponding author, vladimir.katkovnik@tut.fi

## 1 Introduction

In modern science and technology, phase and wavefield imaging are a popular and well established technique for high-accuracy measuring, recording and reconstructing of 2D and 3D objects. The areas of applications are varying from astronomy and engineering to medicine and biology[1,2] . In engineering, phase and wavefield sensing methods serve for nondestructive testing/control and precise measurements (e.g.[3,4]). In medicine and biology, phase measurements are exploited in microscopy and coherent tomography.

Phase imaging is a unique instrument to study details of internal structure of transparent or semitransparent specimens. While only intensity of light fields can be measured, visualization of phase from intensity observations is an important issue. In phase contrast microscopy, methods of wavefront modulation in the Fourier plane have been developed to resolve the visualization problem (Frits Zernike 1930s, Nobel prize 1953). Despite the revolutionary success of these methods

only *qualitative visualization* of phase can be achieved in this way, where features of specimens even visible maybe be so distorted that accurate measurements and even proper interpretations can be problematic.

*Quantitative visualization* is targeted on direct phase imaging and precise phase measuring. Roughly speaking, there are two ways to achieve this goal. The first one is *holography* with measurements given as intensities of the sums of reference and object beams. The second one is *phase retrieval,* treated as an inverse diffusion imaging, essential alternative to holography, which does not require a reference beam. In modern science and technology, the quantitative phase imaging techniques are fundamentally based on digital data processing.

Let us start from the following general formalization of the phase retrieval problem:

$$y_s = |\mathcal{P}_s\{u_o\}|^2,\ s = 1, ..., L, \tag{1}$$

where: $u_o \in \mathbb{C}^{N\times N}$ is an $N \times N$ complex-valued 2D image of an object (specimen); $\mathcal{P}_s$**:** $\mathbb{C}^{N\times N} \longmapsto \mathbb{C}^{M\times M}$ is a complex-valued operator of wavefront propagation from object to sensor plane, $y_s \in \mathbb{R}_+^{M\times M}$ are $M \times M$ intensity images of the wavefronts at the sensor plane.

$L$ experiments are assumed in (1), where $s$ indicates the result for each of them. The equations (1) define relations between the complex-valued wavefronts at the object plane and the power of the wavefronts at the sensor plane. It is convenient to introduce also a notation for the complex-valued wavefront at the sensor plane:

$$u_s = \mathcal{P}_s\{u_o\},\ s = 1, ..., L, \tag{2}$$

The observations for the noiseless case corresponding to (1) are of the form

$$y_s = |u_s|^2,\ s = 1, ..., L, \tag{3}$$

and for noisy observations

$$z_s = \mathcal{G}\{|u_s|^2\},\ s = 1, ..., L, \tag{4}$$

where $\mathcal{G}$ stands for a generator of random observations.

In this paper we assume that the observations have a Poissonian distribution typical for optics with observations based on photon counting.

Reconstruction of the complex-valued object $u_o$ (phase and amplitude) from noiseless or noisy observations is *phase retrieval problem*. Here *phase* emphasizes that the object phase is a variable of the first priority, while the object amplitude is treated as an auxiliary variable often useful only in order to improve phase imaging.

Note, that the term *phase retrieval* is originated from the following mathematical problem. Let $u_s$ be the Fourier transform (FT) of $u_o$, $u_s = \mathcal{F}(u_o)$. If $u_s$ is given, $u_o$ can be precisely calculated as the inverse FT, $u_o = \mathcal{F}^{-1}(u_s)$. Now let the absolute value $|u_s|$ of $u_s$ be given and the phase of $u_s$ is unknown. Is it possible to reconstruct the phase of $u_s$ and in this way the original $u_o$ from the amplitude of FT $|u_s|$ ? In general, the answer is negative and positive only for the special classes of $u_o$, in particular, for the so-called minimum phase signals, or provided some restrictions. In this phase retrieval formulation, the term *phase* points on the phase of the Fourier transform, $u_s$.

In optics, the priority is different. The phase to be retrieved is *phase* of the object $u_o$. The image formation operators $\mathcal{P}_s$ in (1) depend on optical setups. Various methods are developed in

order to make these $\mathcal{P}_s$ sufficiently different for different $s$ and gain *observation diversity*, enabling finding $u_o$ from observations $\{y_s\}_1^L$. Defocussing of the registered images is one of the popular instruments to get a sufficient phase diversity[5–8] . In a recent development a spatial light modulator (SLM) is exploited for defocussing (e.g.[9,10]). The 4f-optical configuration with SLM in the Fourier plane for defocus imitation is proposed in[11] and further studied in[12] .

Random phase modulation of the wavefront is another tool to achieve a desirable phase diversity. It results in observations known as *coded diffraction patterns* (e.g.[13–15]):

$$y_s = |\mathcal{P}\{\mathcal{M}_s \cdot u_o\}|^2, s = 1, ..., L, \tag{5}$$

where $\mathcal{P}$, $\mathbb{C}^{N\times N} \longmapsto \mathbb{C}^{M\times M}$, denotes the propagation operator from the object to sensor planes fixed for all $L$ experiments and the items of the phase masks $\mathcal{M}_s \in \mathbb{C}^{N\times N}$ are complex exponents $\mathcal{M}_s(k,l) = \exp(j\phi_{k,l}(s))$.

The phases $\phi_{k,l}(s)$ in $\mathcal{M}_s$ can be generated as deterministic or random. The phase modulation is able to dramatically change the diffraction pattern of $\mathcal{P}\{u_o\}$ by redistribution of the observed intensities from low to high frequencies.

### *1.1 Phase retrieval algorithms*

There is a growing flow of publications on phase retrieval. Various versions of the Gerchberg-Saxton (GS) techniques are quite universal and applicable for different setups (e.g.[7,8,16–18]). These algorithms based on alternating projections between the object and observations planes allow to incorporate any information available for the variables in these planes. Recent developments in this area as well as a review can be seen in[19] .

Contrary to this type of the intuitive heuristic algorithms the variational formulations have a strong mathematical background and lead to algorithms solving optimization problems. In particular, in[20] one can find constrains sufficient for uniqueness of the solution and algorithms which are very different from GS such as the semidefinite programming phase lifting using matrix completion *(PhaseLift algorithm)*[21] and the greedy sparse phase retrieval (*GESPAR algorithm*)[22] .

There are many publications on revisions of the GS techniques by using optimization formulations. In particular, the links between the conventional GS and variational formulations are studied in[23,24] .

Concerning variational formulations for algorithm design we wish to note the recent Wirtingling flow (WF) and truncated Wirtingling flow (TWF) algorithms[14,25] . Methodologically, these algorithms are developed for the Poissonian likelihood criterion, i.e. for Poissonian noisy observations. Simulation experiments confirm that these algorithm works precisely provided nearly noiseless observations. However, they are not so efficient for noisy observations[26] .

Phase retrieval from coded diffraction patterns of the type (5) is of special interest in the recent publications (e.g.[14,27]). The uniqueness of solution for this scenario is proved in the later paper.

A new variational algorithm for phase retrieval from noisy data based on *transform domain sparsity* for the object phase and amplitude is developed in[26] . Simulation experiments demonstrate that this algorithm enables the accuracy identical to the accuracy of the TWF algorithm for noiseless data and the principal advantage for noisy data. The sparsity concept as a tool for phase retrieval is a topic of the paper[28] , where an original sparsifying learning transform is developed.

The spatial resolution in phase retrieval is limited by two principal factors: low-pass filtering by the propagation operator $\mathcal{P}$ and by pixel size in the pixelated discrete sensor and modulation phase masks. Due to these factors, high-frequency spatial information is lost in intensity observa-

tions, which can be treated as observations of the sub-sampled true object $u_o$. Various methods for super-resolution imaging allowing to compensate these sub-sampling effects are of special interest. One of the straightforward approaches to overcome the pixel size limitations is to use a sequence of laterally shifted holograms (e.g.[29–31]). Compressed sensing (CS) or sparse imaging is a computational approach for restoration of sub-sampled data based on a special mathematical modelling of $u_o$. Applications of this sort of the techniques in optics can be seen in[32–36] .

Other factors limiting the spatial resolution concerns observation errors. First, we need to mention that a Poissonian noise appears due to measurement process in optics counting the photons hitting the sensor. Second, the use of digital camera introduces the readout noise usually modelled by a Gaussian distribution and quantization errors. The later ones can be modelled as a uniform distribution random variables. The quantization effects for phase retrieval are studied[37] , and it is shown that a low-bit quantization may seriously diminish the accuracy of the phase retrieval.

### *1.2 Contribution and structure of this paper*

In this paper we consider phase retrieval from Poissonian noisy phase coded diffraction patterns with the optical setup shown in Fig.1. The complex-valued object $u_o$ to be reconstructed is placed against the SLM applied for phase modulation of the wavefront. A distance between the object and the digital sensor is equal to $2f$, where $f$ is a focal length of the this lens, located in the middle between the object and lens. The system is illuminated by a uniform monochromatic coherent laser beam of wavelength $\lambda$ and intensity equal to $1$. The forward propagation operator $\mathcal{P}$ in (5) is calculated as a rescaled FT, provided that the axial Fresnel approximation for the propagation is assumed. In this setup the object, the SLM and lens are considered as phase transformers of the wavefronts. The Super-Resolution Sparse Phase and Amplitude Reconstruction (SR-SPAR) algo-

rithm proposed in this paper is designed for super-resolution phase/amplitude imaging, which is optimal for Poissonian observations. It is shown by computational experiments that high-accuracy super-resolution reconstructions can be achieved with spacial resolution going up to a quarter of wavelength. The super-resolution GS (SR-GS) algorithm is introduced as a simplified and faster version of SR-SPAR efficient for noiseless data. For the later case, both SR-GS and SR-SPAR demonstrate identical accuracy. SR-SPAR design is based on the methodology developed in[26] for pixel-resolution phase retrieval (SPAR algorithm).

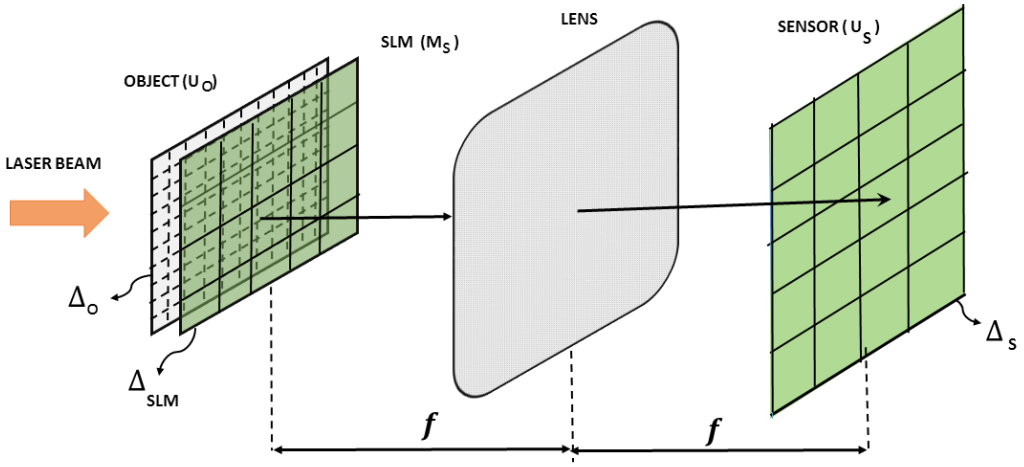


**Fig 1** A sketch of single lens optical setup: Object (o), Spatial light modulator (SLM), Lens and Sensor (s).

This paper is organized as follows. In Subsections 1.3 and 1.4 image formation and noisy observation modeling are presented. The sparsity in the complex domain and the SR-SPAR and SR-GS algorithms are given in Section 2. Section 3 concerns the experimental study of the proposed algorithms.

### *1.3 Image formation*

For wavefront propagation from the object to sensor planes we use the paraxial Fresnel modeling. It gives the following link between the object wavefront $u_o$ and the wavefront at the sensor plane

$u_s$ ([38] , Eq.(5.19)):

$$u_s(\xi,\eta) = \mu \int_{-\infty}^{\infty}\int_{-\infty}^{\infty} u_o(x,y)\mathcal{M}_s(x,y)\exp\{j\frac{-2\pi}{\lambda f}(x\xi + v\eta)\}dxdy, \tag{6}$$

where $\mu = 1/(j \cdot f\lambda)$.

Here $u_o(x,y)$, $u_s(\xi,\eta)$ are complex-valued distributions of the wavefronts at the object plane (lateral coordinates $(x,y)$) and the sensor plane (lateral coordinates $(\xi,\eta)$). $\mathcal{M}(x,y)$ is a complex valued transmission function of SLM. Using FT the input-output model (6) can be given in the form

$$u_s(\xi,\eta) = \mu\mathcal{F}_{u_o\cdot\mathcal{M}_s}(\xi/\lambda f, \eta/\lambda f), \tag{7}$$

where $\mathcal{F}_{u_o\cdot\mathcal{M}}$ stands for FT of the product $u_o(x,y)\mathcal{M}_s(x,y)$.

The formulas (6)-(7) define the forward propagation operator $\mathcal{P}_s$ in Eq.(2). Note, that the model (6) as used in (5) is discrete-continuous with continuous $u_o$ and a physical discretization imposed on $u_s(\xi,\eta)$ by the pixelated sensor and by the pixelated SLM on $\mathcal{M}_s$.

It is useful to mention that the forward propagation (6) is valid also for a single lens system, provided that the lens is located in the object/SLM plane and the distance between this plane and the sensor is equal to $f$.

### *1.4 Poissonian observations*

The measurement process in optics amounts to count the photons hitting the sensor. This process is well modeled by independent Poisson random variables in the following form

$$p(z_s[l] = k) = \exp(-y_s[l]\chi)\frac{(y_s[l]\chi)^k}{k!}, \tag{8}$$

where $p(z_s[l] = k)$ is the probability that the random observation $z_s[l]$ takes integer value $k \geq 0$ and $y_s[l]$ is the intensity of the wavefront at the pixel $l$ defined by (1).

The parameter $\chi > 0$ in (8) is the scaling factor of the Poisson distribution. Recall that the mean and the variance of Poisson random variable $z_s$ are equal and are given by $y_s\chi$, i.e., $E\{z_s\} = \text{var}\{z_s\} = y_s\chi$. Defining the observation signal-to-noise ratio (SNR) as the ratio between the square of the mean and the variance of $z_s$, we have $SNR = E^2\{z_s\}/\text{var}\{z_s\} = y_s\chi$. It follows, that the relative noisiness of observations becomes stronger as $\chi \to 0$ ($SNR \to 0$) and approaches zero when $\chi \to \infty$ ($SNR \to \infty$). The later case corresponds to the noiseless scenario, i.e. $z_s/\chi \to y_s$ with the probability 1.

The scale parameter $\chi$ is of particular importance for modeling as it allows to control the level of noise in the observations.

## 2 Super-resolution sparse phase retrieval

### *2.1 Sparse wavefront representations*

Image sparsity is the commonly observed self-similarity of small fragments (patches) of images, meaning that similar features can be found in patches located in different parts of the image. It follows that an image may admit sparse representations: it can be well approximated by linear combinations of a small number of basic functions. Sparsity has been a hot topic in the last years for various imaging problems (e.g.[39]).

For the complex domain images, such as the object $u_o = B_o \exp(i\varphi_o)$, sparse modeling can be presented in a number of ways essentially different from the methods standard for real-valued variables. This principal difference starts from the fact that $u_o$ is defined by two variables: phase $\varphi_o$ and amplitude $B_o$.

The sparse representation can be imposed on complex-valued $u_o$ directly by using complex-valued basic functions or on the following pairs of real-valued variables:

(1) Phase $\varphi$ (interferometric or absolute) and amplitude $B_o$;

(2) Real and imaginary parts of $u_o$.

Remember that an interferometric (wrapped) phase is restricted to the interval $[-\pi, \pi)$, while an absolute (unwrapped) phase is different by adding an integer number of $2\pi$ to the interferometric phase. In what follows, we denote the interferometric (wrapped) phase of the object as $\varphi_o$ and the corresponding absolute phase as $\varphi_{o,abs}$. We introduce the phase-wrap operator $\mathcal{W} : \mathbb{R} \mapsto [-\pi, \pi)$, linking the absolute and principal phase as $\varphi_o{=}\mathcal{W}(\varphi_{o,abs})$. We also define the unwrapped phase as $\varphi_{o,abs} = \mathcal{W}^{-1}(\varphi_o)$. Notice that $\mathcal{W}^{-1}$ is not an inverse operator for $\mathcal{W}$ because the later is highly non-linear and for signals of dimension two and higher there is no one-to-one relation between $\varphi_{o,abs}$ and $\varphi_o$.

In principle, the absolute phase always can be reconstructed as the interferometric one with the application of unwrapping as post-processing. However, for objects with phase varying beyond the interval $[-\pi, \pi)$, the absolute phase sparse modeling brings essential advantage. It is because, wrapped phases are complicated by fringes, making images more difficult for sparse approximation.

The success of the sparsity approach depends on how rich and redundant are the used dictionaries/transforms (sets of basic functions). In this paper, the sparsity analysis and synthesis is based on the recent, and proved to be very efficient, Block-Matching 3D (BM3D) denoising algorithm[40]

.

Let us mention the basic steps of this advanced technique known as *nonlocal self-similarity sparsity*. At the first stage, the image is partitioned into small overlapping square patches. For

each patch a group of similar patches is collected which are stacked together to form a 3D array (group). This stage is called *grouping*. The entire 3D group-array is projected onto a 3D predefined transform basis. The spectral coefficients obtained as a result of this transform are hard-thresholded (small coefficients are zeroed) and the inverse 3D transform gives the filtered patches, which are returned to the original position of these patches in the image. This stage is called *collaborative* filtering. This process is repeated for all patches of the entire image and obtained overlapped filtered patches are aggregated in the final image estimate. This last stage is called *aggregation*. The details of this algorithm can be seen in[40] .

The links of the BM3D algorithm with the general sparsity concept are revealed in[41] , where it is shown that the *grouping* operations define the data adaptive analysis and synthesis image transforms (frames) and these transforms combined with the thresholding define the thresholding stage of the BM3D algorithm. It is emphasized that sparsity is achieved mainly due to the grouping, which allows the joint analysis of similar patched and, in this way, to guaranty the sparsity (self-similarity of patches), at least for each of the $3D$ groups.

Note that the standard BM3D algorithm, as it is presented in the[40] , is composed of two successive stages: thresholding and Wiener filtering. In this paper we use a simplified version of BM3D, as it is introduced in[41] , including grouping, transforms and thresholding without Wiener filtering.

In what follows, we exploit, for the complex-valued $u_o$, the sparsity imposed on phase and amplitude. The variational formulation for reconstruction of a complex valued $u_o$, optimal for noisy data, results in the likelihood type criteria and optimization with the constrained imposed on sparsity. It has been shown for various optical problems (e.g.[42–44]), that the algorithms are iterative and the sparsity is appeared as BM3D filtering applied separately to estimates of phase and amplitude.

This filtering can be represented in the form:

$$\hat{\varphi}_o = BM3D_{phase}(\varphi_o, th_\varphi), \tag{9}$$

$$\hat{B}_o = BM3D_{ampl}(B_o, th_B), \tag{10}$$

where the filters are applied to the phase and amplitude of $u_o$:

Here $\hat{\varphi}_o$ and $\hat{B}_o$ are sparse approximations of $\varphi_o$ and $B_o$; *phase* and *ampl* as indices of BM3D are used in order to emphasize that the parameters of BM3D can be different for phase and amplitude; $th_\varphi$ and $th_B$ are threshold parameters of the algorithms. The phase in (9) can be interferometric or absolute depending on the sparsity formulation.

The implementation of the sparsity hypothesis in the form of the special filters (9)-(10) is inline with the recent concept *plug-and-play* [45–47] , stating that any efficient filter can serve as a good prior and efficient regularizator in variational design of data processing algorithms.

### *2.2 Super-resolution SPAR algorithm*

#### *2.2.1 Discretization*

The computational wavefront restoration is going from the continuous domain wavefront propagation (7) to the corresponding discrete model based on pixelation of the object $u_o$, thus, we arrive to the discrete modeling of the system linking discrete values of the sensor output (observations) with the discrete values of the object $u_o$.

Conventionally the pixels are square of the size $\Delta_{SLM} \times \Delta_{SLM}$ and $\Delta_s \times \Delta_s$ for the SLM and sensor, respectively. In what follows, for simplicity, $\Delta_{SLM} = \Delta_s$. A continuous object is discretized by pixels of the size $\Delta_o \times \Delta_o$. This discretization is necessary both for digital data

processing as well as for modeling of wavefront propagation and image formation. Contrary to the pixels of SLM and sensor defined by the corresponding optical-electronic devices, the object pixels are *computational*, which maybe be taken arbitrary small.

Assuming for a moment that $\Delta_o = \Delta_s = \Delta_{SLM}$, the reconstruction of $u_o$ from the observations $\{z_s\}$ is the standard phase retrieval problem with an object resolution dictated by the pixel size of the sensor and the SLM.

Let us term this case *pixel-resolution* imaging.

If $\Delta_o < \Delta_s$ we arrive to a much more challenging problem of *pixel super-resolution* or *sub-pixel resolution* imaging. Further, if $\Delta_o$ is so small that $\Delta_o \simeq \lambda$, then it is *wavelength resolution*. Going further to $\Delta_o < \lambda$ we arrive to *sub-wavelength* or *wavelength super-resolution*. The super-resolution phase retrieval with smaller and very small $\Delta_o$ as compared with $\Delta_s$ and $\lambda$ is the goal of this paper.

It is convenient to assume that $\Delta_s = r_s \cdot \Delta_o$, where $r_s \geq 1$ is an integer *pixel super-resolution factor*. In this case, the SLM pixel $\Delta_{SLM} \times \Delta_{SLM}$ covers $r_s^2$ computational object pixels and provides the same modulation phase-shift to all object pixels in this group.

Using for calculation the fast Fourier transform (FFT) we arrive to the discrete analog of (7), within an invariant factor $\mu$, in the form

$$u_s[k,l] = FFT\{u_o[s,t] \cdot \mathcal{M}_s[s,t]\} \frac{\Delta_o^2}{\lambda f}, \tag{11}$$

$$\Delta_s \Delta_o = \frac{\lambda f}{N_D}\,, \tag{12}$$

where $FFT$ stands for 2D FFT and $N_D$ is a side length of a square-support for $[k,l]$ and $[s,t]$.

Here the variables $u_s[k,l]$ and $u_o[s,t] \cdot \mathcal{M}_s[s,t]$ are sampled with the computational period $\Delta_o$.

Then, in particular, the modulation function $\mathcal{M}_s[s,t]$ is a piece-wise invariant with $r_s \times r_s$ squares of invariant values covering the corresponding pixels of SLM.

The constraint (12) is typical for use of FFT for calculation of discrete Fourier transform. All functions and FFT in (11) are calculated for the square support $N_D \times N_D$, where $N_D$ is always higher (even much higher) than the pixelated sizes of the object, the SLM and the sensor.

According to (5), the discrete diffraction pattern is calculated as $y_s[k,l] = |u_s[k,l]|^2$ with the noisy observations obtained according to the Poissonian distribution (8). Note that these computational $y_s[k,l]$ are given with the computational period $\Delta_o$, while the observations are introduced with the sampling period $\Delta_s$. The equations (11)-(12) define the discrete forward propagation model of the system shown in Fig.1. In order to simplify the presentation we preserve the notation $\mathcal{P}$ for this discrete model initially introduced for the continuous domain variables.

### *2.2.2 SR-SPAR algorithm*

The presented SR-SPAR algorithm is derived from the variational formulation introduced for optimal reconstruction of $u_o$ from Poissonian observations $\{z_s[k,l]\}$. The corresponding minus log-likelihood for Poissonian observations according to (8) is as follows

$$\mathcal{L} = \sum_{s=1}^{L} \sum_{k,l} [|u_s[k,l]|^2 \chi - z_s[k,l] \log(|u_s[k,l]|^2 \chi)]. \tag{13}$$

This criterion should be minimized with respect to $u_o[k,l]$, provided the equations (11) linking $u_o$ and $u_s$ and restrictions imposed by the sparsity requirements.

The derivation of the algorithm is similar to the technique developed in[26] for the pixel-resolution phase retrieval. The difference mainly concerns the sampling rates: $\Delta_o = \Delta_s$ in[26] and in this paper

$\Delta_o = \Delta_s / r_s$ meaning that the observations should be upsampled by a factor $r_s$.

We present the SR-SPAR algorithm in the form given in Table 1 referring to[26] . It is emphasized that SR-SPAR, being based on the minimization of (13), is optimal, in the statistical sense, for Poissonian observations.

**Table 1** SR-SPAR Phase Retrieval Algorithm

| | |
|---|---|
| | Input: $\{\tilde{z}_s\}$, $s = 1, ..., L$, $x^1$; |
| | for $t = 1, .., T$; |
| 1. | **Forward propagation**: |
| | $v_s^t = \mathcal{P}\{\mathcal{M}_s \cdot x^t\}$, $v_s^t \in S_D$, $s = 1, ..., L$; |
| 2. | **Poissonian noise suppression**: |
| | $u_s^t = \begin{cases} b_s^t \exp(j \cdot \text{angle}(v_s^t)), v_s^t \in S_S, \\ v_s^t, v_s^t \in S_D \backslash S_S, s = 1, ..., L; \end{cases}$; |
| 3. | **Backward propagation:** |
| | $x^t = \frac{1}{L} \sum_{s=1}^{L} \mathcal{M}_s^* \cdot \mathcal{P}^{-1}\{u_s^t\}$; |
| 4. | **Phase unwrapping:** |
| | $\varphi_{abs}^t = \mathcal{W}^{-1}(angle(x^t))$; |
| 5. | **Sparse phase and amplitude filtering:** |
| | $\varphi_{abs}^{t+1} = BM3D_{phase}(\varphi_{abs}^t, th_\varphi)$, |
| | $B^{t+1} = BM3D_{ampl}(abs(x^t), th_a)$; |
| 6. | **Object wavefront update:** |
| | $x^{t+1} = B^{t+1} \exp(j\varphi_{abs}^{t+1})$; |
| | Output: $\hat{\varphi}_{o,abs} = \varphi_{abs}^{T+1}$, $\hat{B}_o = B^{T+1}$. |

The inputs $\tilde{z}_s$ in this algorithm are the observations $z_s$ upsampled by factor $r_s$. We use the zero-order upsampling giving $\tilde{z}_s$ as piece-wise invariant function with the invariant values for computational pixels corresponding to each of the larger size pixels of the sensor. All calculations in the SR-SPAR algorithm are produced for high-resolution variables with the sampling $\Delta_o$.

At Step 1, the object wavefront estimate $x^t$ is multiplied by the phase mask $\mathcal{M}_s$ and propagated by the operator $\mathcal{P}$ to the sensor plane, with the result denoted as $v_s^t$. These wavefronts are calculated for the diffraction area $N_D \times N_D$ denoted as $S_D$.

At Step 2, the wavefront is updated to the variable $u_s^t$ by filtering the amplitude of $v_s^t$ according

to the given observations $\tilde{z}_s$. The following formula, as derived in[26] , defines the rule on how the updated amplitude $b_s$ is calculated:

$$b_s = \frac{|v_s| + \sqrt{|v_s|^2 + 4\tilde{z}_s\gamma(1+\gamma_1\chi)}}{2(1+\gamma_1\chi)}. \tag{14}$$

These calculations are pixel-wise; $\gamma_1 > 0$ is the parameter of the algorithm. This update is produced provided known observation $\tilde{z}_s$, i.e. for the pixels belonging to the sensor area $S_S$, $v_s \in S_S$. In our modeling the computational diffraction area $S_D$ is always equal or larger than the sensor area, $S_S \subseteq S_D$. For the area out of the sensor, the wavefront values are preserved, $u_s = v_s$ for $v_s \in S_D \backslash S_S$.

At Step 3, the estimates $\{u_s^t\}$ backpropagate to the object plane and update the object wavefront estimate $x^{t+1}$. Here $\mathcal{M}_s^*$ means a complex conjugate $\mathcal{M}_s$ and $\mathcal{P}^{-1}\{u_s^t\} = FFT^{-1}\{u_s^t[k,l]\}\lambda f/\Delta_o^2$.

The sparsification (filtering on the base of sparse approximations) is produced in Step 5. The unwrapping of the phase with reconstruction of the absolute phase in Step 4 is necessary only if the range of the object phase goes beyond $2\pi$.

Following to[26] , we introduce also a simplified version of SR-SPAR named the super-resolution GS algorithm (SR-GS). It differs in two points from SR-SPAR in Table 1: the phase unwrapping and BM3D filtering (Steps 4 and 5) are omitted and the Poissonian filtering in Step 2 is replaced by the rule $b_s \to \sqrt{\tilde{z}_s/\chi}$, which corresponds to the amplitude update standard for the GS style algorithms. This later rule follows from the optimal solution (14) provided that the data is noiseless, i.e. $\chi$ is very large.

It was demonstrated in[42] that using the update shown in Step 2 and different for $v_s^t \in S_D \backslash S_S$ and $v_s^t \in S_S$ allows to improve the accuracy of the wavefront reconstruction. In[48] , this effect is

interpreated as a self-extrapolation of holograms applied for resolution enhancement.

We make publicly available the MATLAB demo-codes http://www.cs.tut./sgn/imaging/sparse of the developed SR-GS and SR-SPAR algorithms, which can be used to reproduce the experiments presented in this paper as well as for further tests.

## 3 Numerical experiments

Both algorithms, SR-SPAR and SR-GS, were tested for various models of $u_o$. In what follows, we are restricted mainly to $256 \times 256$ phase-objects of invariant amplitude and three types of varying phase: test-images Lena normalized to the interval $[0, \pi/2]$; Gaussian shape absolute phase (phase range $50$ radians) and discontinuous Shear Plane (phase range $65$ radians). Respectively, we treat experiments with Lena as interferometric phase imaging, as they do not require phase unwrapping, and experiments with Gaussian and Shear Plane as absolute phase imaging requiring the unwrapping operation in SR-SPAR. The PUMA algorithm[49] is used for phase unwrapping in Step 4 of SR-SPAR.

The fixed parameters of the experiments are: $\Delta_s = \Delta_{SLM} = 5.2\mu m$, $\lambda = 632.8\ nm$, sensor size, in pixels, $4096 \times 4096$, computational diffraction area $S_D$ of size $5120 \times 5120$. The main varying parameters are the computational sampling period $\Delta_o$, the Poissonian noise parameter $\chi$ and computational resolution factor calculated with respect to the sensor as $r_s = \Delta_s/\Delta_o$. It is assumed that $r_s$ is integer and take values $r_s = 1, 8, 16$ and $32$. The $r_s = 1$ corresponds to the pixel-resolution and larger $r_s$ mean super-resolution of the higher order. The sensor of much larger size than the object is taken in order to enable a good quality of super-resolution with large values of the super-resolution factors $r_s$.

It is natural to measure also the super-resolution with respect to the wavelength $\lambda$ as the ratio

$r_\lambda = \Delta_o/\lambda = \Delta_s/(r_s\lambda)$. Then, $r_s = 1$ gives the pixel-resolution with $r_\lambda = 8.21$, i.e. the sensor and SLM pixels are about eight times larger than the wavelength $\lambda$. For $r_s = 8$ we obtain the wavelength resolution with $r_\lambda = 1.03$, the higher values $r_s = 16, 32$ correspond to the sub-wavelength resolution with computational pixels $\Delta_o$ smaller than the wavelength with the wavelength resolution factors $r_\lambda = 0.515$, and $0.257$.

Note that according to the restriction (11) smaller $\Delta_o$ (larger $r_s$) assumes that the lens with a smaller focal distance should be used in the considered optical setup. For the introduced set $r_s$ we obtain the following focal distances $f = [54.7, 6.8, 3.4, 1.7]\ mm$, respectively.

In our experiments the phase modulation masks $\mathcal{M}_s(k,l) = \exp(j\phi_{k,l}(s))$ are random with the Gaussian independent zero-mean phase values, $\phi_{k,l}(s)\tilde{}\mathcal{N}(0, \pi/4)$.

The accuracy of the wavefront reconstruction is characterized by $RMSE$ criteria calculated independently for amplitude and phase. The object phase image can be estimated at least within an invariant global phase-shift $\varphi_{shift}$. It is estimated using as reference the phase of the true object. This correction of the phase is done only for calculation of the criteria and for result imaging and is not used in the algorithm iterations.

In what follows we produce calculations for noisy and nearly noiseless data with the Poissonian scale parameter $\chi$ taking values in the internal $[1,\ 1000]$. The smallest $\chi$ results in the noisiest observations. The corresponding Signal-to-Noise Ratio (SNR) is calculated in $dB$ as

$$SNR = 10\log_{10}(\chi^2 \sum_{s=1}^{L} ||y_s||_F^2 / \sum_{s=1}^{L} ||y_s\chi - z_s||_F^2)\ dB. \tag{15}$$

For the super-resolution experiments we use the objects with a fixed number of computational pixels of size $\Delta_o = \Delta_s/r_s$, thus larger $r_s$ means a smaller physical size of the object. The success-

ful super-resolution imaging, in particular the wavelength resolution, requires a sensor size being much larger than the object size.

### *3.1 Modulation phase mask and sparsity*

Let us start from qualitative observations concerning the effects of the basic ingredients of the considered setup and the developed algorithm. Fig.2 shows the reconstruction of the object phase for noiseless data ($\chi = 1000$), provided that only a single experiment is produced, $L = 1$. The left image shows the true phase. The next completely destroyed image in Fig.2 is obtained from the experiment with no phase modulation and without the sparse modeling for phase and amplitude. Thus, the diffraction pattern is a squared amplitude of FT of the object complex exponent. The third image is obtained from a single experiment, where the phase modulation is employed and no BM3D filters are used (SR-GS algorithm). This modulation makes the main features of the phase distribution at least visible but quite noisy. This noise is a result of the used phase modulation. The fourth image is obtained by the SR-SPAR algorithm, i.e. with phase modulation and BM3D filtering for the phase and amplitude. It shows nearly perfect reconstruction of the object phase.

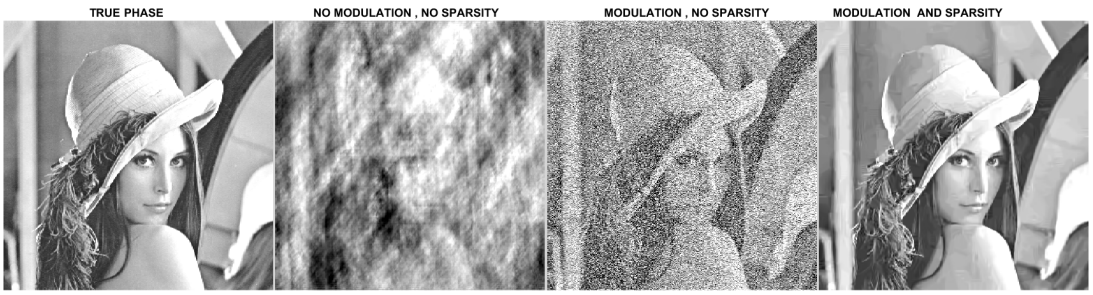


**Fig 2** Phase reconstructions from left-to-right: (a) true Lena image, (b) reconstruction without phase modulation and BM3D filtering, (c) reconstruction with phase modulation but without BM3D filtering (SR-GS), (d) reconstruction with phase modulation and with BM3D filtering (SR-SPAR), $L = 1$, $\chi = 1000$.

For a larger number of experiments ($L > 1$) the accuracy of the phase reconstruction with the phase modulation is improves quickly both for processing with SR-SPAR and with SR-GS. Fig.2

and above comments are given for the pixel-resolution imaging, $r_s = 1$, and for nearly noiseless observations.

### *3.2 Super-resolution for interferometric phase*

The reconstruction results for the Lena phase test-image with super-resolution factor $r_s = 8$ are shown in Figs.3 and 4. The cross-sections for phase and amplitude are shown for middle horizontal lines, where the red (solid) and blue (dotted) curves correspond to the reconstructions and true images, respectively. The reconstructions in Fig.3 are of the high accuracy. They are obtained for the low level noise ($\chi = 1000$, $SNR = 60$ dB). The results in Fig.4 are much worse but we need take into account that the observations are very noisy ($\chi = 1$, $SNR = 30.5$ dB) for super-resolution with the factor $r_s = 8$. Thus, we can treat these results as of acceptable quality. It can be noted that the low level noise reconstruction is, visually, nearly perfect. The accuracy of reconstruction is good for both phase and amplitude. The experiments produced for higher order resolution (not shown) demonstrate a noticeable degradation of results for $r_s = 16$ and fail completely for $r_s = 32$.

### *3.3 Absolute phase imaging*

SR-SPAR phase imaging for *Shear Plane* phase distribution $(256 \times 256)$ with the maximum value of about $65$ rad is shown in Figs.5-7. In Fig.5 the results are shown for the resolution factor $r_s = 8$. Visually, the obtained 3D surface is very close to the true one, thus, it is not necessary to show it. The 2D images in these figures show the wrapped phase and amplitude reconstructions. As it is seen from the wrapped phase, the errors in the reconstruction can be noticed. Nevertheless, the quality of this super-resolution reconstruction is very good. In Fig.6, the similar results are shown

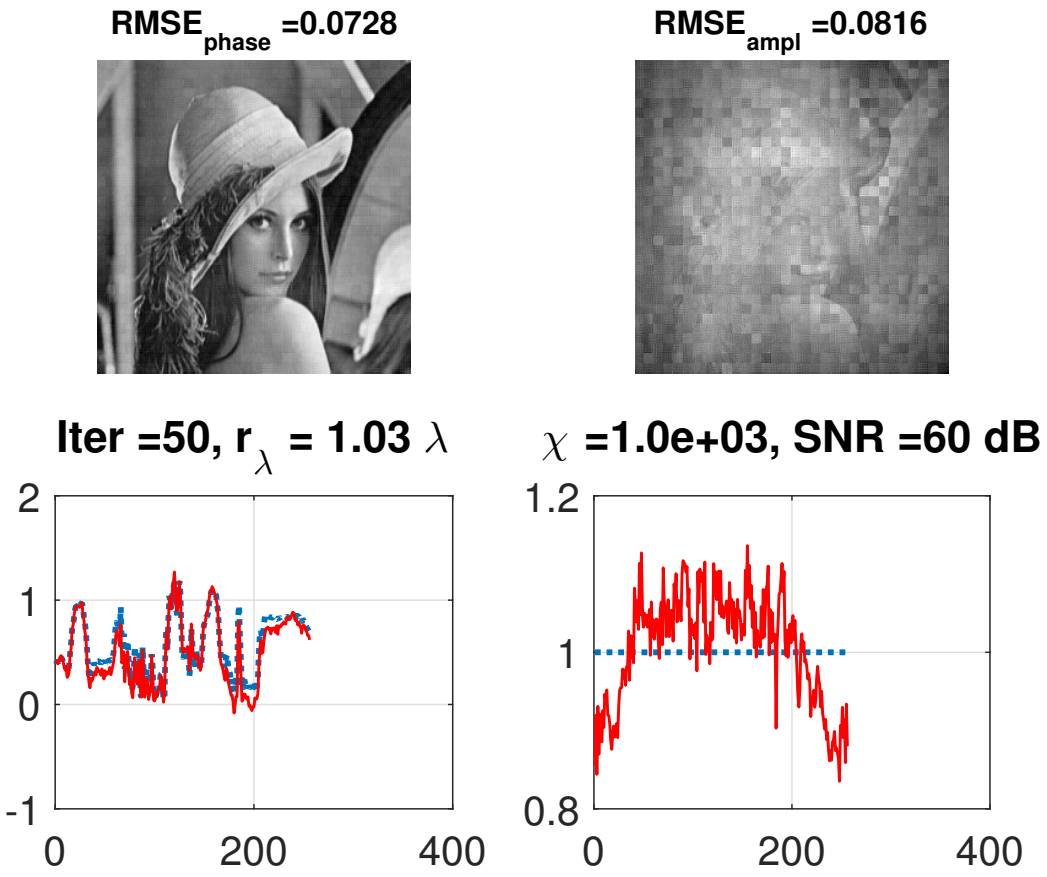


**Fig 3** SR-SPAR, Lena phase image and amplitude reconstructions: super-resolution with $r_s = 8$, for nearly noiseless observations, $\chi = 1000$. In the cross-sections (middle horizontal line), the solid (red) curves are for the reconstructions and the dotted (blue) ones for the true data.

for the much higher resolution factor $r_s = 16$. The shown 3D surface is of a quite acceptable quality, while the wrapped phase and amplitude reconstruction, shown as 2D images, definitely demonstrate that these results are of a much lower quality than those achieved for $r_s = 8$. In the final Fig.7 we show the attempt to get reconstruction for the super-resolution factor $r_s = 32$. These results are definitely negative, the phase reconstruction failed.

Phase imaging for *Gaussian* phase distribution $(256 \times 256)$ with maximum value of about $50$ rad is shown in Figs.8-9. The reconstructions are obtained for quite noisy data $\chi = 100$ and the super-resolution factors $r_s = 8$ and $r_s = 16$. For $r_s = 8$ (Fig.8) the quality of the reconstruction is very good and the 3D phase reconstruction is very close to the true Gaussian phase object. The

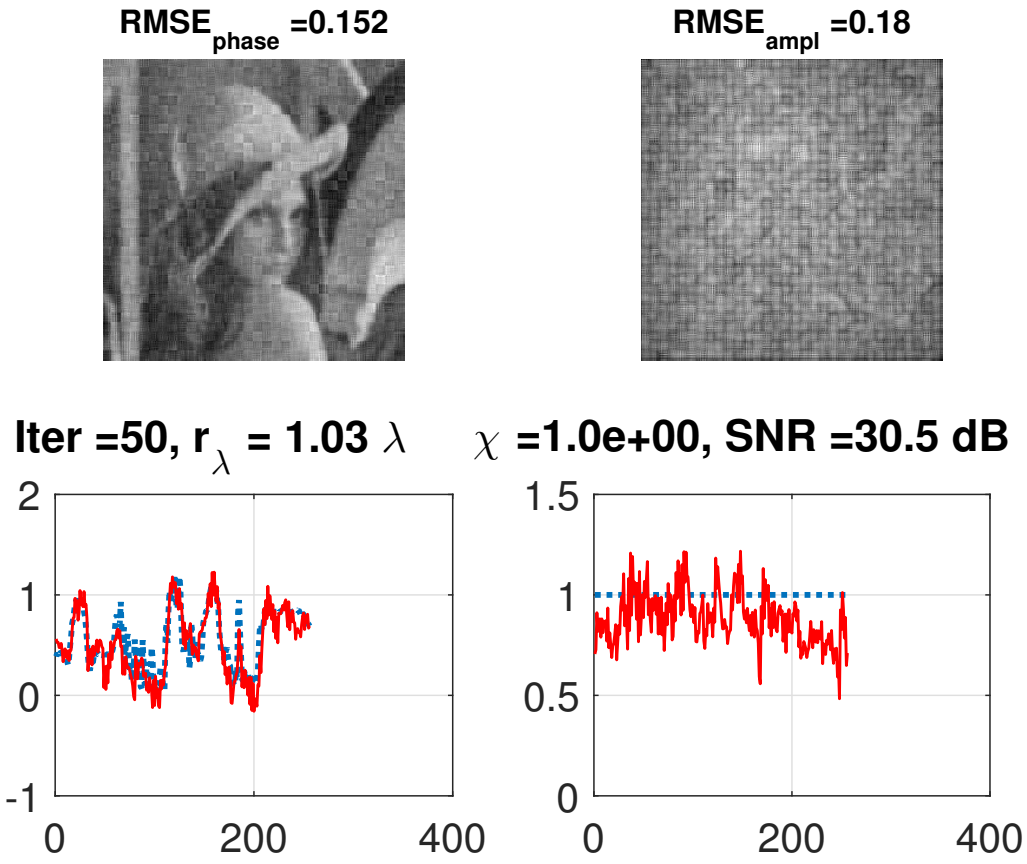


**Fig 4** SR-SPAR, Lena phase image and amplitude reconstructions: super-resolution with $r_s = 8$, noisy observations, $\chi = 1$. In the cross-sections (middle horizontal line), the solid (red) curves are for the reconstructions and the dotted (blue) ones for the true data.

situation becomes much worse for the super-resolution factor $r_s = 16$ (Fig.9). The errors in the phase reconstruction are obvious and quite large. The attempt to get reconstruction for the super-resolution factor $r_s = 32$ failed and we do not show these images.

In conclusion of this subsection we wish to note that we are talking about very high levels of the pixel super-resolution $r_s = 8$ and $r_s = 16$ corresponding to the wavelength and half wavelength super-resolution.

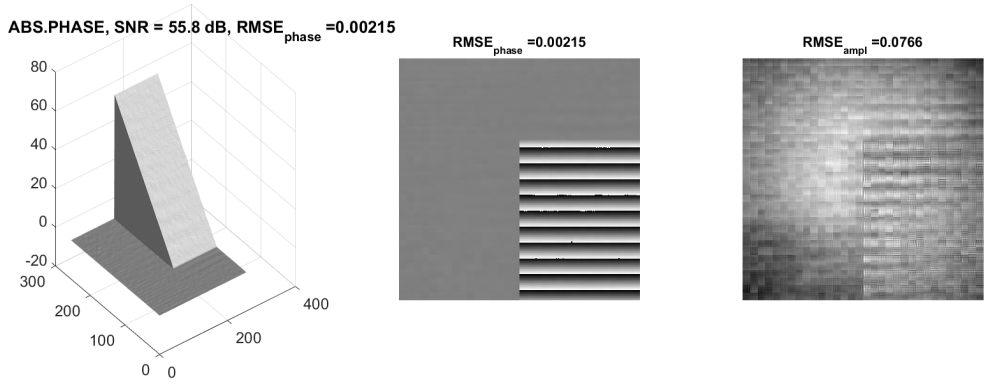


**Fig 5** SR-SPAR, Shear Plane phase image, phase and amplitude reconstructions: nearly noiseless data, $\chi = 1000$. The super-resolution reconstruction is produced for $r_s = 8$. The 3D image is very close to the true phase image. The 2D images are given for the wrapped phase and amplitude reconstructions.

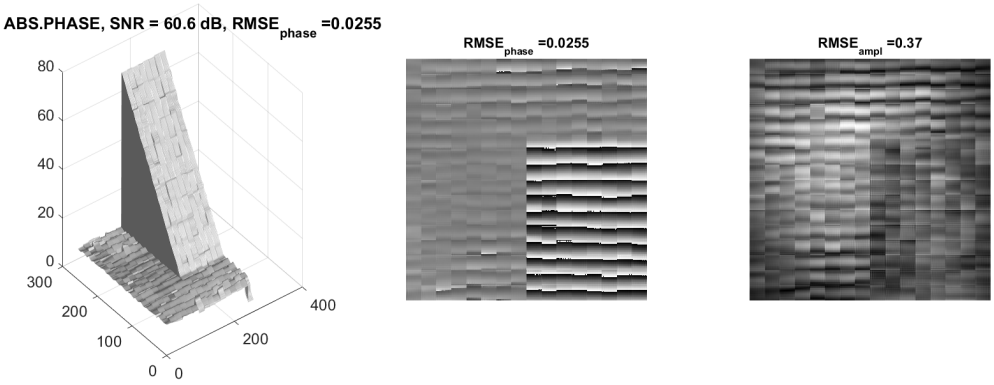


**Fig 6** SR-SPAR, Shear Plane phase image, phase and amplitude reconstructions: nearly noiseless data, $\chi = 1000$. The super-resolution reconstruction is produced for $r_s = 16$. The 2D images are given for the wrapped phase and amplitude reconstructions. The 3D image surface is covered by well seen square blocks $16 \times 16$. This discretization of the surface is due to SLM pixels having size $16 \times 16$ in the computational pixels.

### *3.4 More on sub-wavelength resolution*

Let us demonstrate a few interesting tests on sub-wavelength imaging with $r_s = 32$ corresponding to $r_\lambda = 0.257$ with the object size $128 \times 128$.

In Figs.10 and 11 the reconstructions for the two-peak phase object are shown. The four squares clearly seen in the amplitude reconstructions are patterns of four pixels of SLM each covering $32 \times 32$ computational pixels of the object. These images confirms that the both developed algorithms SR-GS and SR-SPAR are able to reconstruct two point-wise phase peaks separated by the distance

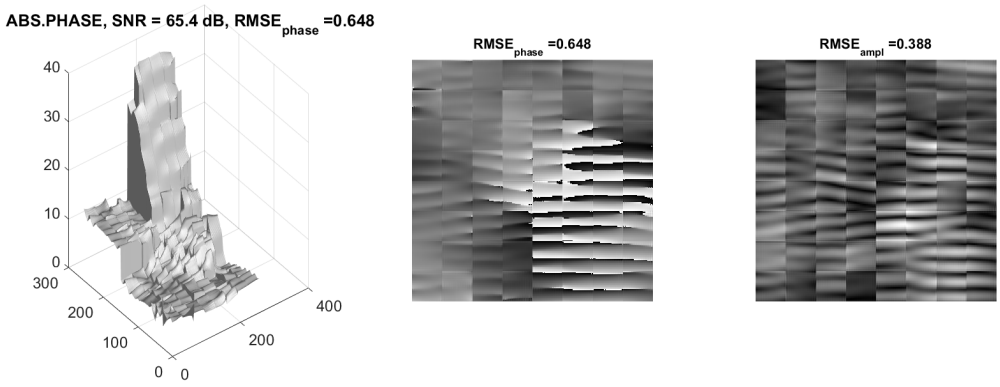


**Fig 7** SR-SPAR, Shear Plane phase image, phase and amplitude reconstructions: nearly noiseless data, $\chi = 1000$. The super-resolution reconstruction is produced for $r_s = 32$. The 2D images are given for the wrapped phase and amplitude reconstructions. The algorithm failed.

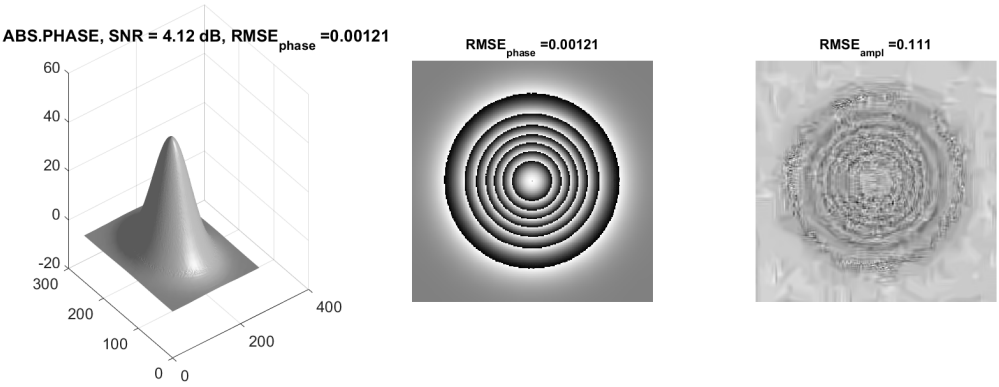


**Fig 8** SR-SPAR, Gaussian Plane phase image, phase and amplitude reconstructions: noisy data, $\chi = 100$. The super-resolution reconstruction is produced for $r_s = 8$. The 2D images are given for the wrapped phase and amplitude reconstructions.

equal to $0.257\lambda$. It is a demonstration of the sub-wavelength resolution.

### *3.5 Parameters of the SR-SPAR algorithm*

The performance of the SR-SPAR algorithm essentially depends on its parameters. Optimization can be produced for each magnitude/phase distribution and noise level. However, in our experiments, the parameters are fixed. The image patches in $BM3D$ are of size $8 \times 8$. The group size is limited to $39$ patches. The step size between the neighboring patches is equal to $3$. The transforms DCT (for patches) and Haar (for the group length) are used for 3D group data processing in

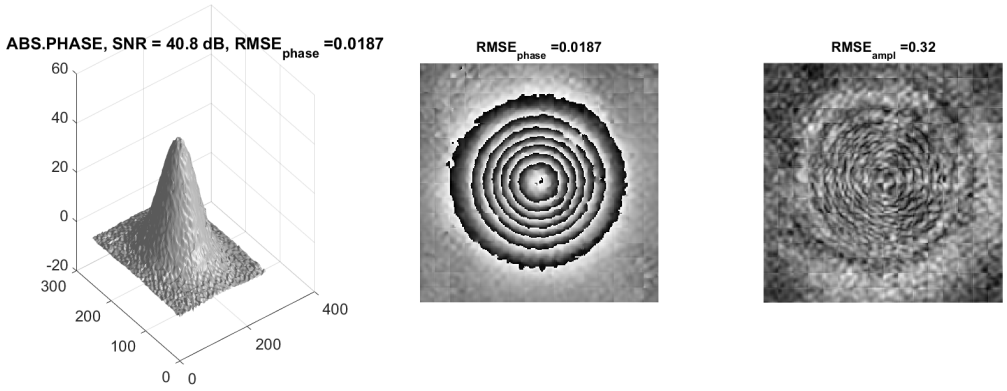


**Fig 9** SR-SPAR, Gaussian Plane phase image, phase and amplitude reconstructions: noisy data, $\chi = 100$. The super-resolution reconstruction is produced for $r_s = 16$. The 2D images are given for the wrapped phase and amplitude reconstructions.

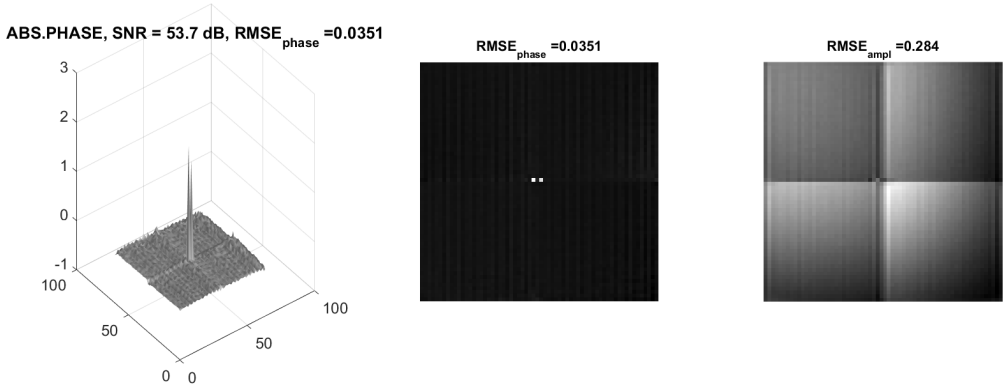


**Fig 10** Two-picks reconstructions, SR-GS algorithms: distance between peaks $0.257\ \lambda$, $\chi = 1000$. The four $32 \times 32$ squares well seen in the amplitude reconstruction correspond to four pixels of SLM.

$BM3D$. In the shown results as an initial guess for the iterative SR-GS and SR-SPAR algorithm we use an image with the invariant amplitude equal to $1.3$ and zero phase.

The parameters defining the iterations of the algorithm are as follows: $\gamma_1 = 1/\chi$; $th_a = 4.0$; $th_\varphi = 4.0$. The number of the iterations is fixed to $50$.

For our experiments we use MATLAB R2015a and a computer with the processor Intel(R) Core(TM) i7-4800MQ@ 2.7 GHz.

The complexity of the algorithm is characterized by the time required for processing. For $50$ iterations, $L = 12$ and $256 \times 256$ images this time is as follows: SR-GS$\simeq 2500$ sec.; SR-SPAR

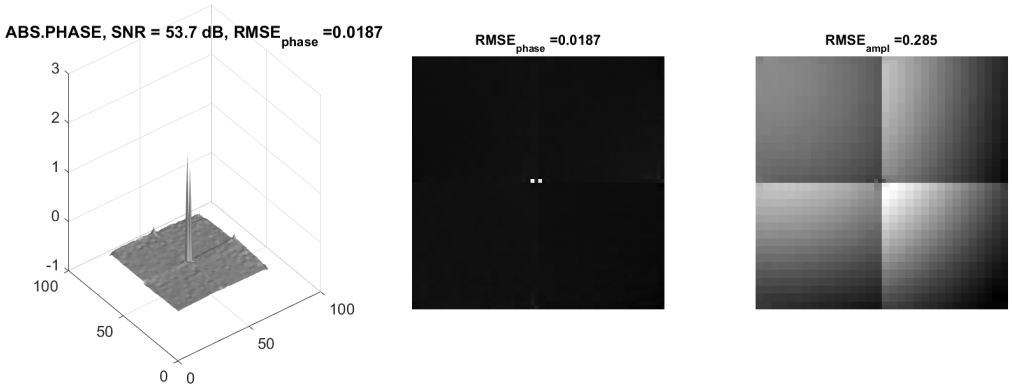


**Fig 11** Two-picks reconstructions, SR-SPAR algorithms: distance between peaks $0.257\ \lambda$, $\chi = 1000$. The four $32 \times 32$ squares well seen in the amplitude reconstruction correspond to four pixels of SLM.

without phase unwrapping $\simeq 3300$ sec; SR-SPAR with phase unwrapping $\simeq 1500$ sec.

## 4 Conclusion

Computational super-resolution phase retrieval is considered for phase-coded intensity observations. The proposed algorithm is derived as an optimal solution for Poissonian noisy observations. One of the essential instruments of the algorithm is a sparsity hypothesis applied to both phase and amplitude. The efficiency of the algorithm is confirmed by simulation experiments. It is shown that high level super-resolution can be achieved with the pixel super-resolution factor up to 32, i.e. the pixel size of the reconstructed object in 32 times smaller that the pixel size of the sensor and the SLM. In comparison with the wavelength, the super-resolution up to one quarter of the wavelength is demonstrated.

## 5 Acknowledgment

This work is supported by Academy of Finland, project no. 287150, 2015-2019.

*References*

1 R. K. Tyson, *Principles of adaptive optics*, CRC press (2015).

2 L. V. Wang and H.-i. Wu, *Biomedical optics: principles and imaging*, John Wiley & Sons (2012).

3 B. C. Kress and P. Meyrueis, *Applied Digital Optics: from micro-optics to nanophotonics*, John Wiley & Sons (2009).

4 J. Gluckstad and D. Palima, *Generalized Phase Contrast: Applications in Optics and Photonics*, Springer (2009).

5 D. Misell, "An examination of an iterative method for the solution of the phase problem in optics and electron optics: I. test calculations," *Journal of Physics D: Applied Physics* **6**(18), 2200 (1973).

6 W. Saxton, "Correction of artifacts in linear and non-linear high-resolution electron-micrographs," *Journal de microscopie et de spectroscopie electroniques* **5**(5), 665–674 (1980).

7 G. Pedrini, W. Osten, and Y. Zhang, "Wave-front reconstruction from a sequence of interferograms recorded at different planes," *Optics letters* **30**(8), 833–835 (2005).

8 P. Almoro, G. Pedrini, and W. Osten, "Complete wavefront reconstruction using sequential intensity measurements of a volume speckle field," *Applied optics* **45**(34), 8596–8605 (2006).

9 C. Kohler, F. Zhang, and W. Osten, "Characterization of a spatial light modulator and its application in phase retrieval," *Applied optics* **48**(20), 4003–4008 (2009).

10 L. Camacho, V. Micó, Z. Zalevsky, *et al.*, "Quantitative phase microscopy using defocusing by means of a spatial light modulator," *Optics express* **18**(7), 6755–6766 (2010).

11 C. Falldorf, M. Agour, C. v. Kopylow, *et al.*, "Phase retrieval by means of a spatial light

modulator in the fourier domain of an imaging system," *Applied optics* **49**(10), 1826–1830 (2010).

12 V. Katkovnik and J. Astola, "Phase retrieval via spatial light modulator phase modulation in 4f optical setup: numerical inverse imaging with sparse regularization for phase and amplitude," *JOSA A* **29**(1), 105–116 (2012).

13 P. F. Almoro, G. Pedrini, P. N. Gundu, *et al.*, "Enhanced wavefront reconstruction by random phase modulation with a phase diffuser," *Optics and Lasers in Engineering* **49**(2), 252–257 (2011).

14 E. J. Candes, X. Li, and M. Soltanolkotabi, "Phase retrieval from coded diffraction patterns," *Applied and Computational Harmonic Analysis* **39**(2), 277–299 (2015).

15 P. F. Almoro, Q. D. Pham, D. I. Serrano-Garcia, *et al.*, "Enhanced intensity variation for multiple-plane phase retrieval using a spatial light modulator as a convenient tunable diffuser," *Optics letters* **41**(10), 2161–2164 (2016).

16 P. F. Almoro, A. M. S. Maallo, and S. G. Hanson, "Fast-convergent algorithm for speckle-based phase retrieval and a design for dynamic wavefront sensing," *Applied optics* **48**(8), 1485–1493 (2009).

17 R. W. Gerchberg, "A practical algorithm for the determination of phase from image and diffraction plane pictures," *Optik* **35**, 237–246 (1972).

18 J. R. Fienup, "Phase retrieval algorithms: a comparison," *Applied optics* **21**(15), 2758–2769 (1982).

19 C. Guo, S. Liu, and J. T. Sheridan, "Iterative phase retrieval algorithms. i: optimization," *Applied optics* **54**(15), 4698–4708 (2015).

20 Y. Shechtman, Y. C. Eldar, O. Cohen, *et al.*, "Phase retrieval with application to optical imaging: a contemporary overview," *IEEE Signal Processing Magazine* **32**(3), 87–109 (2015).

21 E. J. Candes, Y. C. Eldar, T. Strohmer, *et al.*, "Phase retrieval via matrix completion," *SIAM review* **57**(2), 225–251 (2015).

22 Y. Shechtman, A. Beck, and Y. C. Eldar, "Gespar: Efficient phase retrieval of sparse signals," *IEEE transactions on signal processing* **62**(4), 928–938 (2014).

23 J. R. Fienup, "Phase-retrieval algorithms for a complicated optical system," *Applied optics* **32**(10), 1737–1746 (1993).

24 H. H. Bauschke, P. L. Combettes, and D. R. Luke, "Phase retrieval, error reduction algorithm, and fienup variants: a view from convex optimization," *JOSA A* **19**(7), 1334–1345 (2002).

25 Y. Chen and E. Candes, "Solving random quadratic systems of equations is nearly as easy as solving linear systems," in *Advances in Neural Information Processing Systems*, 739–747 (2015).

26 V. Katkovnik, "Phase retrieval from noisy data based on sparse approximation of object phase and amplitude,"

27 A. Fannjiang, "Absolute uniqueness of phase retrieval with random illumination," *Inverse Problems* **28**(7), 075008 (2012).

28 Q. Lian, B. Shi, and S. Chen, "Transfer orthogonal sparsifying transform learning for phase retrieval," *Digital Signal Processing* **62**, 11–25 (2017).

29 W. Bishara, U. Sikora, O. Mudanyali, *et al.*, "Holographic pixel super-resolution in portable lensless on-chip microscopy using a fiber-optic array," *Lab on a Chip* **11**(7), 1276–1279 (2011).

30 K. Guo, S. Dong, P. Nanda, *et al.*, "Optimization of sampling pattern and the design of fourier ptychographic illuminator," *Optics express* **23**(5), 6171–6180 (2015).

31 A. Greenbaum, W. Luo, B. Khademhosseinieh, *et al.*, "Increased space-bandwidth product in pixel super-resolved lensfree on-chip microscopy," *Scientific reports* **3** (2013).

32 S. Gazit, A. Szameit, Y. C. Eldar, *et al.*, "Super-resolution and reconstruction of sparse sub-wavelength images," *Optics Express* **17**(26), 23920–23946 (2009).

33 M. Marim, E. Angelini, J.-C. Olivo-Marin, *et al.*, "Off-axis compressed holographic microscopy in low-light conditions," *Optics letters* **36**(1), 79–81 (2011).

34 Y. Rivenson, A. Stern, and B. Javidi, "Compressive fresnel holography," *Journal of Display Technology* **6**(10), 506–509 (2010).

35 Y. Rivenson, A. Stern, and J. Rosen, "Compressive multiple view projection incoherent holography," *Optics express* **19**(7), 6109–6118 (2011).

36 J. Song, C. L. Swisher, H. Im, *et al.*, "Sparsity-based pixel super resolution for lens-free digital in-line holography," *Scientific reports* **6** (2016).

37 A. M. S. Maallo, P. F. Almoro, and S. G. Hanson, "Quantization analysis of speckle intensity measurements for phase retrieval," *Applied optics* **49**(27), 5087–5094 (2010).

38 J. W. Goodman, *Introduction to Fourier optics*, Roberts and Company Publishers (2005).

39 M. Elad, *Sparse and Redundant Representations: from Theory to Applications in Signal and Image Processing*, Springer (2010).

40 K. Dabov, A. Foi, V. Katkovnik, *et al.*, "Image denoising by sparse 3-D transform-domain collaborative filtering," *IEEE Transactions on image processing* **16**(8), 2080–2095 (2007).

41 A. Danielyan, V. Katkovnik, and K. Egiazarian, "BM3D frames and variational image deblurring," *IEEE Transactions on Image Processing* **21**(4), 1715–1728 (2012).

42 V. Katkovnik and J. Astola, "High-accuracy wave field reconstruction: decoupled inverse imaging with sparse modeling of phase and amplitude," *JOSA A* **29**(1), 44–54 (2012).

43 V. Katkovnik and J. Astola, "Compressive sensing computational ghost imaging," *JOSA A* **29**(8), 1556–1567 (2012).

44 V. Katkovnik and J. Astola, "Sparse ptychographical coherent diffractive imaging from noisy measurements," *JOSA A* **30**(3), 367–379 (2013).

45 F. Heide, M. Steinberger, Y.-T. Tsai, *et al.*, "Flexisp: A flexible camera image processing framework," *ACM Transactions on Graphics (TOG)* **33**(6), 231 (2014).

46 S. Sreehari, S. Venkatakrishnan, B. Wohlberg, *et al.*, "Plug-and-play priors for bright field electron tomography and sparse interpolation," *IEEE Transactions on Computational Imaging* **2**(4), 408–423 (2016).

47 C. A. Metzler, A. Maleki, and R. G. Baraniuk, "Bm3d-prgamp: Compressive phase retrieval based on bm3d denoising," in *Image Processing (ICIP), 2016 IEEE International Conference on*, 2504–2508, IEEE (2016).

48 T. Latychevskaia and H.-W. Fink, "Resolution enhancement in digital holography by self-extrapolation of holograms," *Optics express* **21**(6), 7726–7733 (2013).

49 J. M. Bioucas-Dias and G. Valadao, "Phase unwrapping via graph cuts," *IEEE Transactions on Image processing* **16**(3), 698–709 (2007).

**Vladimir Katkovnik** received Ph.D. (1964) and D.Sc. degrees (1974) in Technical Cybernetics from Leningrad Polytechnic Institute (LPI. From 1964 to 1991, he was an Associate Professor and

then a Professor with the Department of Mechanics and Control Processes, LPI. Since 2003, he is with the Department of Signal Processing, Tampere University of Technology, Finland. He published 6 books and over 350 refereed journal and conference papers. His research interests include stochastic image/signal processing, nonparametric estimation, computational imaging, computational phase imaging.

**Karen Egiazarian (Eguiazarian)** received the M.Sc. degrees (1981) from Yerevan State University, in 1981, the Ph.D. degree from Moscow State University, Russia (1986) and the DTech degree from Tampere University of Technology (TUT), Finland (1994). He is a Professor leading the Computational Imaging Group, Signal Processing Laboratory, TUT. He has authored about 650 refereed journal and conference papers. His research interests include computational imaging, sparse coding, image and video restoration. He serves as an Associate Editor for the IEEE Transactions of Image Processing and is the Editor-in-Chief of the Journal of Electronic Imaging.

# List of Figures

3 SR-SPAR, Lena phase image and amplitude reconstructions: super-resolution with $r_s = 8$, for nearly noiseless observations, $\chi = 1000$. In the cross-sections (middle horizontal line), the solid (red) curves are for the reconstructions and the dotted (blue) ones for the true data.

4 SR-SPAR, Lena phase image and amplitude reconstructions: super-resolution with $r_s = 8$, noisy observations, $\chi = 1$. In the cross-sections (middle horizontal line), the solid (red) curves are for the reconstructions and the dotted (blue) ones for the true data.

5 SR-SPAR, Shear Plane phase image, phase and amplitude reconstructions: nearly noiseless data, $\chi = 1000$. The super-resolution reconstruction is produced for $r_s = 8$. The 3D image is very close to the true phase image. The 2D images are given for the wrapped phase and amplitude reconstructions.

6 SR-SPAR, Shear Plane phase image, phase and amplitude reconstructions: nearly noiseless data, $\chi = 1000$. The super-resolution reconstruction is produced for $r_s = 16$. The 2D images are given for the wrapped phase and amplitude reconstructions. The 3D image surface is covered by well seen square blocks $16 \times 16$. This discretization of the surface is due to SLM pixels having size $16 \times 16$ in the computational pixels.

7 SR-SPAR, Shear Plane phase image, phase and amplitude reconstructions: nearly noiseless data, $\chi = 1000$. The super-resolution reconstruction is produced for $r_s = 32$. The 2D images are given for the wrapped phase and amplitude reconstructions. The algorithm failed.

# List of Tables